Journal of Hydroinformatics

Journal of Hydroinformatics Vol 25 No 6, 2268 doi: 10.2166/hydro.2023.042

Hydrodynamics of laminar pipe flow through an extended partial blockage by CFD

Nuno M. C. Martins [a,b,*], Dídia I. C. Covas [b], Silvia Meniconi [a], Caterina Capponi [a] and Bruno Brunone [a]

[a] Department of Civil and Environmental Engineering, The University of Perugia, Perugia, Italy
[b] CERIS, Instituto Superior Técnico, Universidade de Lisboa, Lisbon, Portugal
*Corresponding author. E-mail: nunomiguelmartins@tecnico.ulisboa.pt

NMCM, 0000-0003-4994-673X; DICC, 0000-0001-6901-4767; SM, 0000-0001-7843-7147; CC, 0000-0002-5308-5189; BB, 0000-0002-7106-2116

ABSTRACT

In this paper, an advanced three-dimensional (3D) computational fluid dynamics (CFD) model is used to analyse the steady-state hydrodynamics of laminar flow through an extended partial blockage (PB) in a pressurised pipe. PB corresponds to one of the main faults affecting pipelines. In fact, it reduces its carrying capacity with economic consequences, and as it does not give rise to any external evidence, its detection can be very challenging. The performance of the model is evaluated by comparing the numerical results with the available experimental data from the literature. Subsequently, the velocity and pressure distributions are analysed, and the main features of the flow field are described in terms of both local and global dimensionless parameters. Furthermore, the behaviour of the discharge coefficient is also investigated. The obtained results confirm that steady-state measurements can identify the presence of PB and follow its evolution over time but cannot detect its location and size. On the other hand, the location and severity of PBs can be provided by means of transient tests.

Key words: computational fluid dynamics (CFD), laminar flow, partial blockage, pipes, thick-walled orifice

HIGHLIGHTS

- Analysis of the steady-state laminar flow through an extended partial blockage.
- Validation of a 3D CFD model of an extended partial blockage with experimental data from the literature.
- Velocity and pressure fields characterisation around an extended partial blockage.
- Characterisation and evaluation in time of an extended partial blockage.
- Hydrodynamics of a flow through an extended partial blockage.

1. INTRODUCTION

Pressurised pipe systems allow conveying fluids – such as water, gas, and oil – over long distances; in addition, the venous and arterial systems can also be assimilated into them. In pipe systems, partial blockages – hereafter referred to as PBs – may result from the deposition of sand and excess calcium, in the case of water pipes, and hydrates, paraffin and asphaltene, in the case of refined and crude oil pipes; plaques and clot may happen in the venous and arterial systems. PBs may also result from simultaneous processes with solid deposition triggered by the previous formation of other solids (i.e., asphaltene or hydrates after wax deposition). PBs start from small growths in the roughness of inner pipe walls and, if not detected and addressed early on, they continue to grow and protrude transversely and longitudinally. Consequently, they may encroach on a significant part of the cross-sectional area of the pipe (Duan *et al.* 2015). In subsea pipelines, as an example, the cold temperature of the pipeline walls causes the wax particles in the oil to crystallise and accumulate over time on the inner pipe walls, eventually leading to a PB and potentially complete blockage, if left untreated. The circumferential shape of 'natural' PBs is quite common as the result of a radial protrusion. PBs may also be due to mechanical causes, such as collapsed pipes or negligently partially closed in-line valves. Due to such a variety of causes of formation, PBs can occur anywhere in the pipelines. PBs are such a widespread concern, that they are considered the most insidious fault to detect and manage, in both water and petroleum industries.

In gravity systems, PBs reduce the carrying capacity of the pipes, leading to a smaller discharge, whereas, in rising mains, they increase energy consumption and cause safety risks due to pressure build-up. This is also the case of plaques in the

arterial system if left undetected and untreated. Accordingly, early detection is considered the best approach for maintenance purposes.

Since PBs do not provide external evidence (unlike, as an example, leaks), their detection and characterisation, i.e., the evaluation of their size and location is an arduous challenge. In addition, considering the fact that, in most cases, pipelines are buried, any intervention is highly expensive and time-consuming. Furthermore, the 'nature' of the PB – i.e., its consistency (hardness) – plays a crucial role in identifying the most appropriate rehabilitation technique. If the PB cannot be removed by local flushing/chemical injection, then the blocked pipeline section must be completely replaced. In pipelines conveying liquids, on which attention is focused in this paper, several methods have been proposed for detecting PBs: vibration analysis (Lile *et al.* 2012), pulse-echo methodology (Duan *et al.* 2015), acoustic reflectometry (Papadopoulou *et al.* 2008), pressure measurements in steady- (Yang *et al.* 2019), and unsteady-state flows (Meniconi *et al.* 2011; Duan *et al.* 2014; Louati *et al.* 2018). The last method is discussed here in more detail as connected to this paper.

Detection methods by using pressure unsteady-state measurements, the so-called transient test-based techniques (TTBTs), are based on the properties of the pressure waves generated by a manoeuvre (Meniconi *et al.* 2018; Keramat *et al.* 2019). Such pressure waves travel along the pipeline, back and forward, reflected by any anomaly (e.g., leaks and PBs), as well as boundaries. The location of any anomaly, and then a PB, can be determined on the basis of the timing of the reflected pressure wave measured at suitable sections. Accordingly, this technique is also called time-domain reflectometry. The performance of TTBTs depends significantly on the modalities of transient tests. In particular, the characteristics of the generated pressure wave – the sharper, the better (Brunone *et al.* 2021) – the accuracy of the pressure transducers, the frequency of sampling – the higher, the better – and the steadiness of the pre-transient flow conditions play an important role (Meniconi *et al.* 2016). Precisely, as shown in Brunone *et al.* (2021), for a given measurement section, the smaller the value of the pre-transient Reynolds number, the easier the evaluation of the reflected pressure wave. Accordingly, as a pre-transient condition, it is appropriate to set a very small value of the Reynolds number corresponding to a small value of the mean velocity, for a given liquid and internal pipe diameter. Such a circumstance makes laminar flow very attractive as an appropriate pre-transient condition.

Within TTBTs, according to the mentioned mechanisms of interaction between pressure waves and PBs, a distinction can be made between 'discrete' and 'extended' PBs in terms of their length (Brunone *et al.* 2008). Precisely, at a partially closed in-line valve or local diameter reduction, as examples of discrete PBs, the incoming pressure wave gives rise to a single reflected pressure wave. On the other hand, in the case of a small bore pipe, as an example of the extended PBs, the transient response is bell-shaped (Meniconi *et al.* 2012). In such a latter feature, the pressure rise is due to the interaction of the incoming pressure wave with the shrinkage of the opening area, whereas the successive pressure drop is generated by the interaction with the expansion of the opening area. An alternative terminology defines 'discrete' and 'extended' PBs as 'sharp-edged' and 'thick-walled' (or 'short tubes') orifices, respectively.

This paper aims to accurately simulate the pressure and velocity distribution around an extended PB by means of a three-dimensional (3D) computational fluid dynamics (CFD) model. The performance of the model is evaluated on the basis of the experimental data available in the literature. As pointed out above, attention is focused on laminar flow conditions. The rationale for this approach is that the use of one-dimensional (1D) model results is quite inadequate since only the mean values of the pressure and velocity are provided. As a consequence, the 1D approach prevents the identification of possible complex structures (i.e., eddies) downstream of the PB that qualify the flow field and influence the interaction mechanisms with the pressure waves. On the other hand, the 3D CFD model allows capturing in any detail the pressure and velocity distribution around the PB, both upstream and downstream. With respect to Martins *et al.* (2021) – where the PB length is assumed as negligible and then a sharp-edged orifice is considered – in this paper, a much more complex flow field is explored, which indeed resembles real extended PBs.

This paper is organised as follows. The quantities that characterise the hydrodynamic behaviour of extended PBs, as well as experimental data used to validate the performance of the 3D CFD model, are reported in Section 2, along with a description of the 3D CFD model, with attention to the setup and convergence assessment phases. In Section 3, firstly, the 3D CFD model results are compared with the selected experimental data. Subsequently, the numerical model is used to highlight the main features of the flow through extended PBs for different flow conditions and geometric characteristics. In such a context, the weakness of the approach based on steady-state pressure measurements is pointed out. Finally, Section 4 summarises the main conclusions about the 3D CFD model results.

2. METHODS

2.1. Flow through extended partial blockages

As mentioned, in this section, attention is focused on the analysis of the available experimental results concerning extended PBs in laminar conditions. Subsequently, such results are used for evaluating the performance of the 3D CFD model.

According to Tu *et al.* (2006), any feature, Ψ, characterising the steady-state hydrodynamics of the flow through extended PBs can be expressed by means of the following dimensionless relationship (Figure 1):

$$\Psi = f(\phi, \beta, Re, Eu, C_d) \tag{1}$$

where ϕ is the length-to-diameter ratio,

$$\phi = \frac{L}{d} \tag{2}$$

with L is the PB length measured in the flow direction, and d is the orifice's inner diameter (aperture). The diameter ratio, β, is given by:

$$\beta = \frac{d}{D} \tag{3}$$

with D representing the pipe's inner diameter. The Reynolds number describes the flow in the pipe:

$$Re = \frac{UD}{\nu} \tag{4}$$

with U being the mean flow velocity in the pipe, and ν being the fluid kinematic viscosity; alternatively, the orifice Reynolds number, $Re_d (=Re/\beta = U_d d/\nu$, with U_d being the mean velocity at the orifice) is also used. The Euler number,

$$Eu = \frac{2\beta^4 \Delta p}{\rho U^2} \tag{5}$$

takes into account the 'net pressure drop' (Figure 1) through the orifice (Hasegawa *et al.* 1997), Δp, with ρ being the fluid

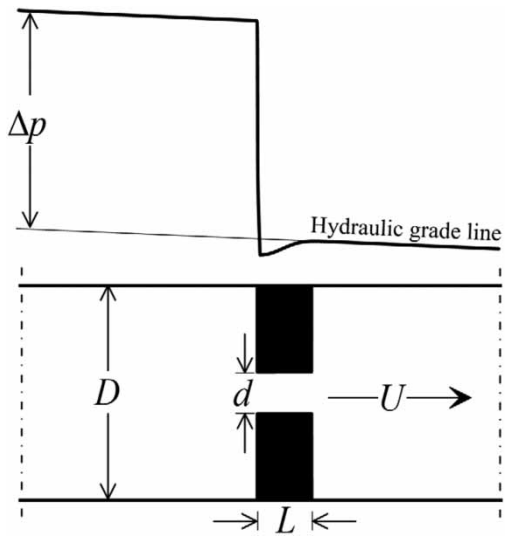

Figure 1 | Schematics of an extended partial blockage (PB).

density. The discharge coefficient, C_d, describes globally the flow through PBs:

$$C_d = \frac{U}{\beta^2}\sqrt{\rho\frac{(1-\beta^4)}{2\Delta p}} \tag{6}$$

whereas the global local energy dissipation can be evaluated by considering the local head loss coefficient:

$$k = \frac{2\Delta p}{\rho U^2} \tag{7}$$

that is linked to Eu by the following relationship:

$$Eu = k\beta^4 \tag{8}$$

According to the value of ϕ, orifices are classified into: (i) sharp-edged: $\phi \leq 0.125$; (ii) thick-walled: $0.125 < \phi < 2$; and (iii) short tubes: $\phi \geq 2$ (Tu *et al.* 2006; Jankowski *et al.* 2008).

In Martins *et al.* (2021), for sharp-edged orifices, the performance of the 3D CFD model was tested based on laboratory data provided by Zampaglione (1969), Johansen (1997), Jankowski *et al.* (2008), and Alvi *et al.* (1978). On the other hand, as mentioned, this paper focuses on thick-walled orifices and short tubes (both assimilable to extended PBs).

As a necessary premise, it is the case to point out the quite small number of laboratory tests available in the literature for laminar flow conditions. Moreover, only global quantities – i.e., C_d and Eu– and not pressure or velocity distributions – are provided. Accordingly, there are considered data from the experiments executed by Hasegawa *et al.* (1997), Kiljanski (1993), and Sahin & Ceyhan (1996), whose main characteristics are synthesised in Table 1.

2.2. CFD model

In this section, the governing equations and open-source software OpenFOAM (OF) 3D CFD model are described.

2.2.1. Governing equations

The Navier–Stokes (N-S) equations are derived from the conservation principles of mass and momentum to simulate the fluid flow. The mass conservation principle for a compressible fluid is expressed by the following continuity equation (Fay 1994):

$$\frac{D\rho}{Dt} + \rho\frac{\partial u_k}{\partial x_k} = 0 \tag{9}$$

where t is the time, and u_k is the velocity components in the spatial coordinate x_k (with $k = 1, 2, 3$). The conservation of momentum principle gives rise to the Cauchy equations:

$$\rho\frac{Du_i}{Dt} = \frac{\partial \sigma_{ij}}{\partial x_j} + \rho f_m \tag{10}$$

where σ is the Cauchy stress tensor, and f_m is the mass forces per unit mass acting on the fluid.

Table 1 | Experimental setups and parameters in previous studies

	Diameter ratio	Length-to-diameter ratio	Orifice Reynolds number
Hasegawa *et al.* (1997)	$\beta \leq 0.1$	$0.092 \leq \phi \leq 1.14$	$2 \leq Re_d \leq 717$
Kiljanski (1993)	$\beta \leq 0.12$	$\phi = 0.5, \quad \phi = 1$	$0.01 \leq Re_d \leq 462$
Sahin & Ceyhan (1996)	$\beta = 0.5$	$0.06 \leq \phi \leq 1$	$1 \leq Re_d \leq 148$

The fluid constitutive equations relate the stress tensor to velocity gradients, describing the rheological behaviour of fluids. For an isotropic, homogeneous, and Newtonian fluid, the stress tensor constitutive equations are:

$$\sigma_{ij} = -p\delta_{ij} + \xi\delta_{ij}\frac{\partial u_k}{\partial x_k} + \mu\left(\frac{\partial u_i}{\partial x_j} + \frac{\partial u_j}{\partial x_i}\right) \tag{11}$$

where p is the thermodynamic pressure, δ_{ij} is the Kronecker function, μ is the dynamic viscosity, and ξ (=− 2/3) is the second viscosity coefficient. Inserting Equation (11) – i.e., the stress–strain law – in the momentum equation, yields the general form of the N-S equations for an isotropic and Newtonian fluid:

$$\rho\frac{Du_i}{Dt} = \rho f_{mi} - \frac{\partial p}{\partial x_i} - \frac{\partial}{\partial x_i}\left(\xi\frac{\partial u_k}{\partial x_k}\right) + \frac{\partial}{\partial x_j}\left[\mu\left(\frac{\partial u_i}{\partial x_j} + \frac{\partial u_j}{\partial x_i}\right)\right] \tag{12}$$

To close the problem, initial and boundary conditions are needed to be specified in space and time (Denton & Dawes 1998).

2.2.2. Model setup

3D CFD simulations, carried out using OF, involve three key stages: pre-processing, simulation, and post-processing.

The pre-processing stage includes the fluid domain definition, mesh generation and model setup, with the definition of boundaries and solver parameters.

SnappyHexMesh, the mesh generation tool, considers a mesh generated in the blockMesh tool and a geometry shape by a computer-aided design software. Then, the generated cylinder mesh is sculpted and refined, adjusting it to the extended PB, i.e., a concentric orifice with specific length and diameter. In the simulations below, a 4-m pipe with an inner diameter $D = 0.02$ m is considered, with the concentric orifice placed in the mid-length of the pipe (Figure 2).

The mesh used in the simulations considers the parameters, η_a, η_c, and η_r proposed by Martins *et al.* (2014), with $\eta_a = 0.57$, $\eta_c = 0.009$, and $\eta_r = 0.0005$, where the subscripts a, c, and r indicate the axial, circumferential, and radial direction, respectively. Since high-velocity gradients are expected, meshes herein present a much larger number of cells with respect to Martins *et al.* (2014), with mesh refinements not only at the PB but also in the zone near it. This is a necessary premise for the following simulation in transient conditions. In fact, even though the upstream flow is laminar, downstream of the PB the flow is much more complex, with recirculation and consequently large circumferential eddies (Zampaglione 1969; Martins *et al.* 2021). This points out the necessity for extra mesh refinements to capture the interaction with the travelling pressure waves, such as those generated for the PB detection. The assumed boundaries conditions are defined in Figure 2: the constant pressure at the inlet, the no-slip condition at pipe walls, and the velocity distribution at the outlet. The local head loss completes (Figure 2) at a distance downstream of the PB equal to the length of the expansion cone, X^*, where the flow reattaches the pipe wall. The flow region downstream of the PB (coloured in dark grey in Figure 2), surrounded by swirls, is called '*corrente viva*'. The area of the '*corrente viva*', A_v, increases with the distance from the orifice; at X^*, it is $A_v = A$, with A being the pipe cross-sectional area. The pre-processing stage divides the fluid domain into smaller, non-overlapping subdomains generating a mesh of cells in which Equations (9) and (10) will be numerically solved in the next stage. In the second stage, in OF, the N-S equation and continuity equations are solved by the pressure-based solver rhoSimpleFoam, within the finite volume method. RhoSimpleFoam considers the relationship between pressure and velocity adjustments to carry out the mass conservation to obtain the pressure field. The convergence of the numerical solution can be assessed by progressively tracking the

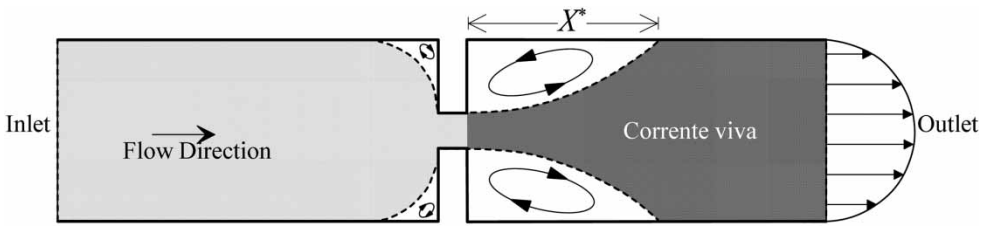

Figure 2 | Schematics of the hydrodynamics of an extended PB.

imbalances (residuals). This imbalance measures the overall conservation of the flow properties. The solution is assumed to have converged when the residual values drop below 10^{-7}. Finally, in the third stage – the post-processing stage, the obtained results, validated by considering the available experimental data, allow analysing the flow upstream and downstream of the PB in detail.

3. RESULTS AND DISCUSSION

3.1. CFD results vs. selected experimental data

As anticipated, the performance of the 3D CFD is evaluated by considering the experimental results mentioned in Section 2. In Figures 3 and 4, the values of C_d given by the 3D CFD model are compared with the experimental ones provided by Sahin & Ceyhan (1996) and Kiljanski (1993), respectively. In both cases, the numerical results are in excellent agreement with the experimental data. As an example, for the Sahin and Ceyhan data, the average relative error is equal to 3.4, 6.7, and 6.02%, for flow conditions of Figure 3(a)–3(c), respectively.

Encouraging results are also obtained in terms of the value of the *Eu* as shown in Figure 5, where the 3D CFD results are compared with the experimental data from Hasegawa *et al.* (1997).

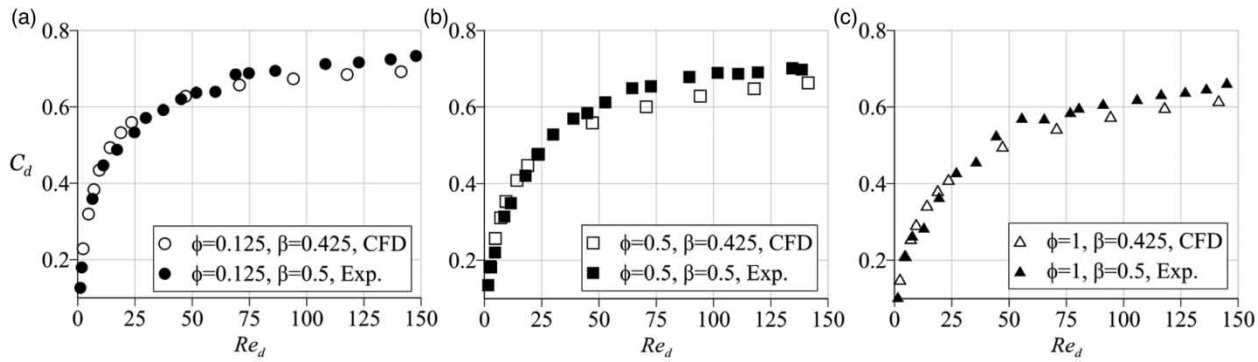

Figure 3 | Dependence of C_d on Re_d 3D CFD results vs. experimental data from Sahin & Ceyhan (1996): (a) $\phi = 0.125$; (b) $\phi = 0.5$; and (c) $\phi = 1$.

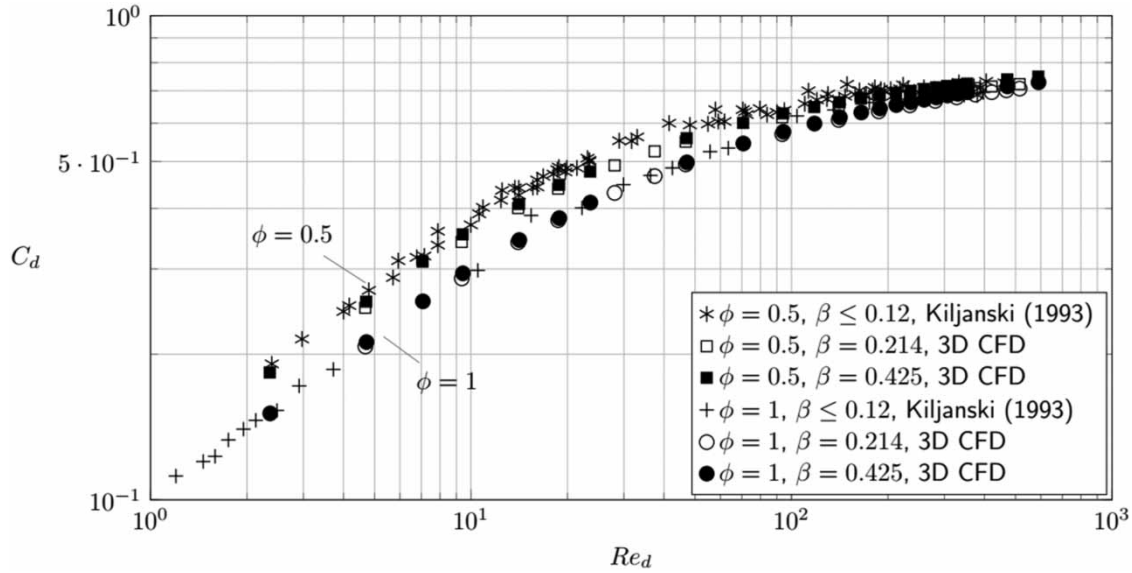

Figure 4 | Dependence of C_d on Re_d: experimental data from Kiljanski (1993) vs. 3D CFD results.

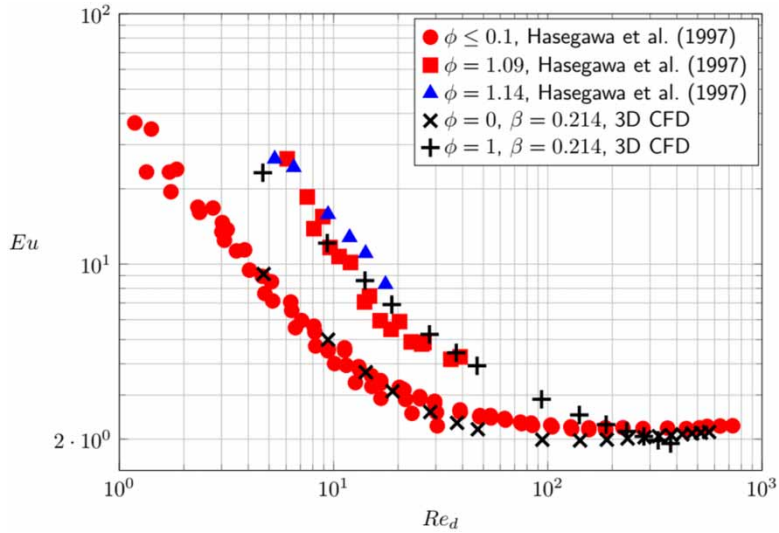

Figure 5 | Dependence of *Eu* on the Re_d. Experimental data from Hasegawa *et al.* (1997) vs. 3D CFD results.

The above positive results in terms of the performance of the 3D CFD model authorise exploring both the global (e.g., in terms of k values) and local (i.e., in terms of pressure and velocity distributions) behaviour of extended PBs.

3.2. Simulated scenarios

3D CFD simulations concerned three values of β(=0.214, 0.425, and 0.697) for both thick-walled ($\phi = 0.125$, 0.5, and 1) and short-tube orifices ($\phi = 2$, and 5). In terms of *Re*, the numerical experiments range between 1 and 350; for each β, the maximum value of *Re* is smaller than the critical value, Re_{crit}, i.e., the value above which pulsating phenomena occur (Zampaglione 1969). Precisely, it is $110 < Re_{crit} < 120$ for $\beta = 0.214$; $250 < Re_{crit} < 300$ for $\beta = 0.425$; and $350 < Re_{crit} < 400$ for $\beta = 0.697$. The main characteristics of the numerical simulations are reported in Table 2.

3.3. The global behaviour of extended PBs

Having in mind the need to identify a viable procedure for the characterising PBs, the behaviour of k, defined by Equation (7), is discussed here. With this aim, in Figure 6, the values of k for a range of values of *Re*, ϕ, and β are reported.

From this plot, it emerges the indelible mark of PBs in terms of the local head loss. However, the steady-state measurements do not allow identifying nor the length, ϕ, nor the severity, β, of the PB. In fact, for a given *Re*, if an unexpected Δp is measured between two sections, it is not possible characterising the PB. In fact, a given value of k may be due to different values of β and ϕ. In other words, steady-state measurements allow identifying the existence of a PB, following its evolution in time, but not detecting its location and size. Such a result implies the need of using TTBTs for PBs identification and characterisation.

3.4. Flow field analysis

In this section, the flow field characteristics are analysed in detail by considering representative values of *Re*, ϕ, and β. In this context, firstly, the behaviour along the pipe axis of the relevant pressure and velocity distribution is shown. Accordingly, in

Table 2 | Main characteristics of the numerical simulations

Diameter to ratio	Length-to-diameter ratio	Reynolds number
$\beta = 0.214$	$\phi = 0.125; 0.5; 1; 2; 5$	$1 \leq Re \leq 110$
$\beta = 0.425$		$1 \leq Re \leq 250$
$\beta = 0.697$		$1 \leq Re \leq 350$

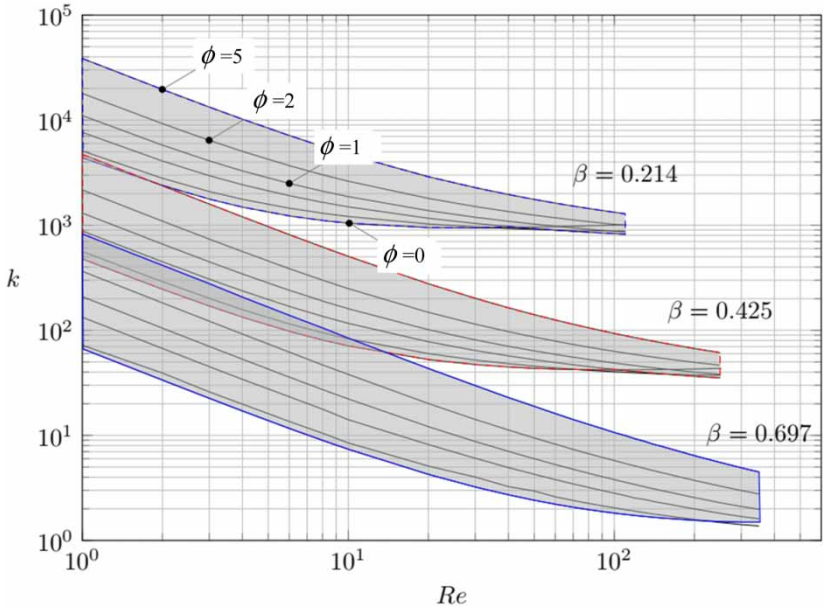

Figure 6 | Local head loss coefficient,k, for given values of the length-to-diameter ratio, ϕ, and diameter ratio, β, vs. Reynolds number,Re.

Figures 7–9, the pressure and velocity contours are reported in the upper and lower part, respectively. In Figure 7, for given ϕ(=0.5) and β(=0.425), different values of Re are considered (=50, 100 and 150).

In Figure 8, ϕ(=0.5) and Re(=100) are kept constant, whereas the value of β varies (=0.214, 0.425, and 0.697). In Figure 9, constant values of β(=0.425) and Re(=100) are assumed, for different values of ϕ(=0.5, 1, and 2).

At a glance, no noticeable difference can be observed between the above contours, from the qualitative point of view. A quantitative analysis has then been executed. With this aim, in Figure 10, the behaviour of the dimensionless parameters $u* = u/u_0$, and $p* = p/p_0$ vs. $x/X*$ has been considered, with u_0 (p_0) being the axial local velocity (pressure) at $x = 0$. Inspection of Figure 10 allows stating that the shape of the curves is the same regardless of the value of the parameters ϕ, β, and Re. A further confirmation is offered by curves in Figures 11–13, where the behaviour along the pipe axis of the following global parameters is reported:

$$\alpha = \frac{\int_A u^3 \mathrm{d}A}{U^3 A} \tag{13}$$

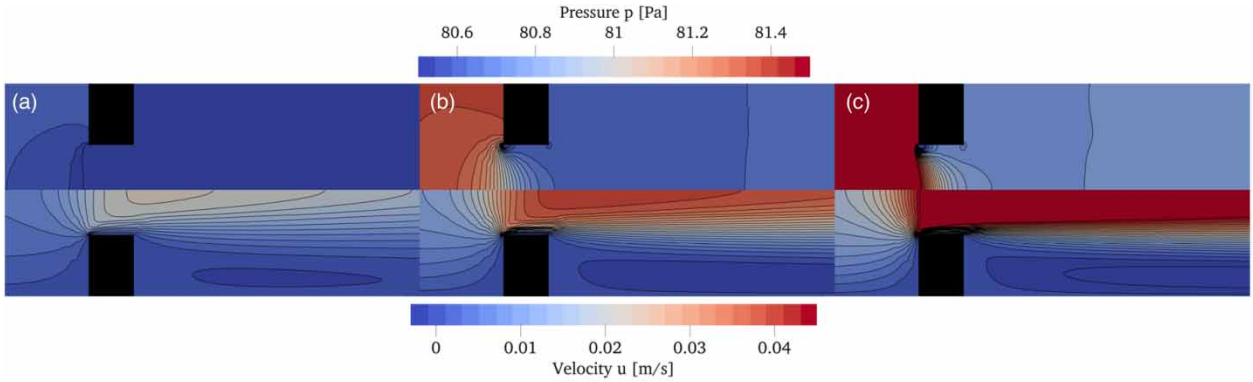

Figure 7 | Contours of pressure (upper part) and velocity (lower part) along the pipe axis, for $\phi = 0.5$ and $\beta = 0.425$: (a) $Re = 50$; (b) $Re = 100$; and (c) $Re = 150$.

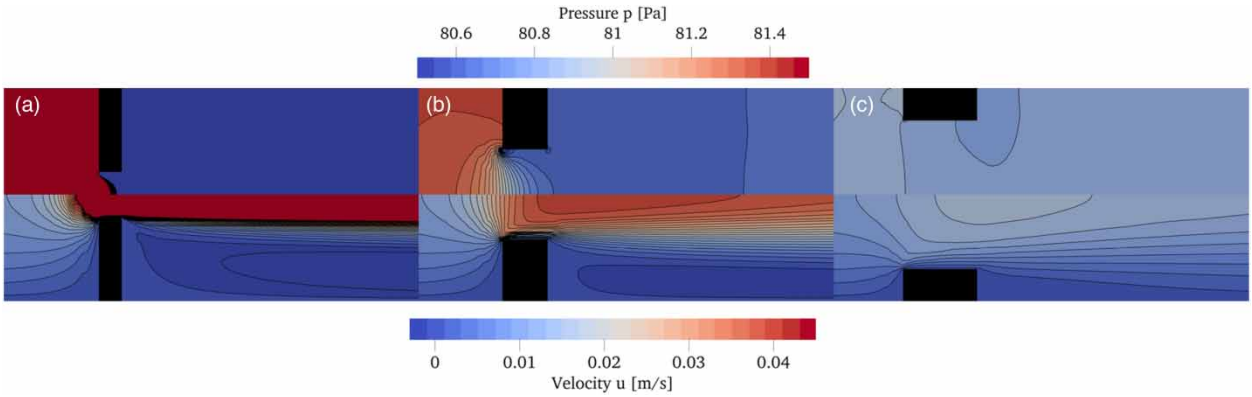

Figure 8 | Contours of pressure (upper part) and velocity (lower part) along the pipe axis, for $\phi = 0.5$ and $Re = 100$: (a) $\beta = 0.214$; (b) $\beta = 0.425$; and (c) $\beta = 0.697$.

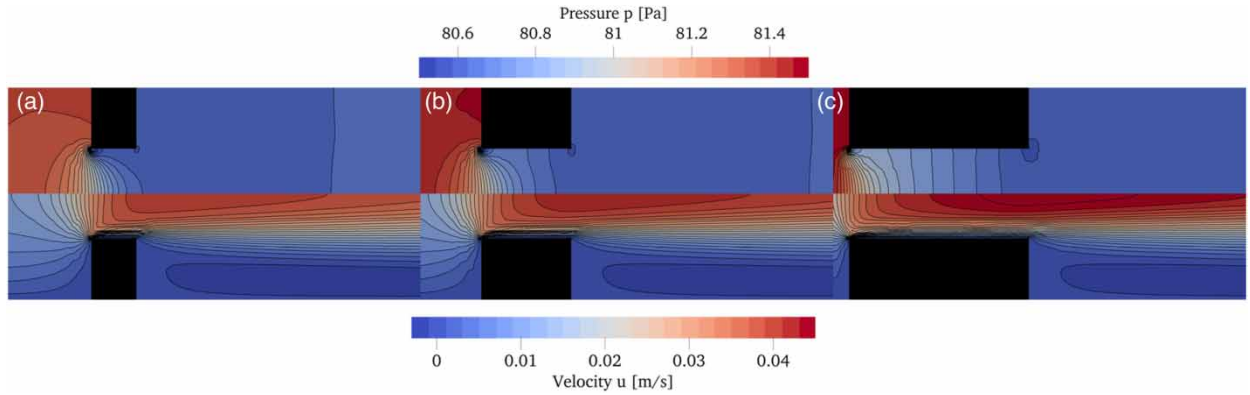

Figure 9 | Contours of pressure (upper part) and velocity (lower part) along the pipe axis, for $\beta = 0.425$ and $Re = 100$: (a) $\phi = 0.5$; (b) $\phi = 1$; and (c) $\phi = 2$.

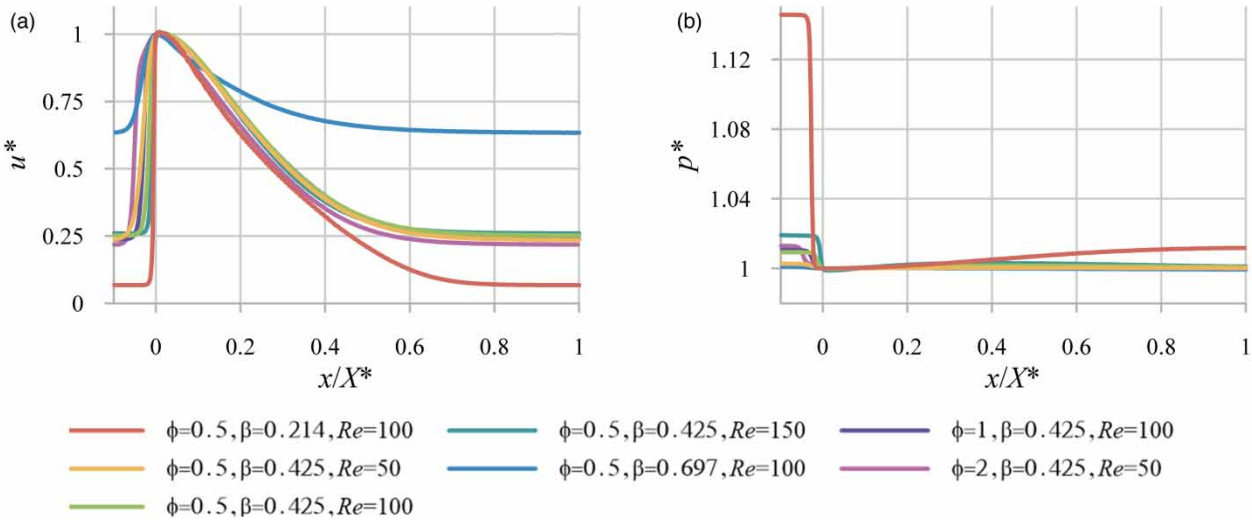

Figure 10 | Behaviour of the dimensionless axial velocity and pressure.

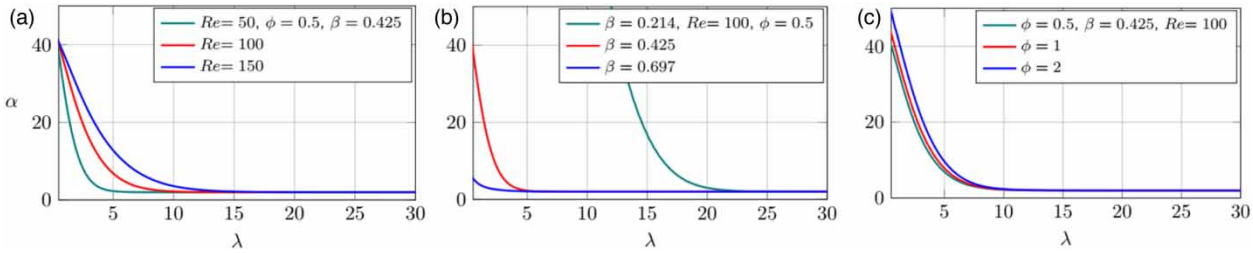

Figure 11 | Kinetic energy correction factor for: (a) $Re = 50$, 100, and 150, with $\phi = 0.5$, and $\beta = 0.425$; (b) $\beta = 0.214$, 0.425, and 0.697, with $\phi = 0.5$ and $Re = 100$; and (c) $\phi = 0.5$, 1 and 2, $\beta = 0.425$, and $Re = 100$.

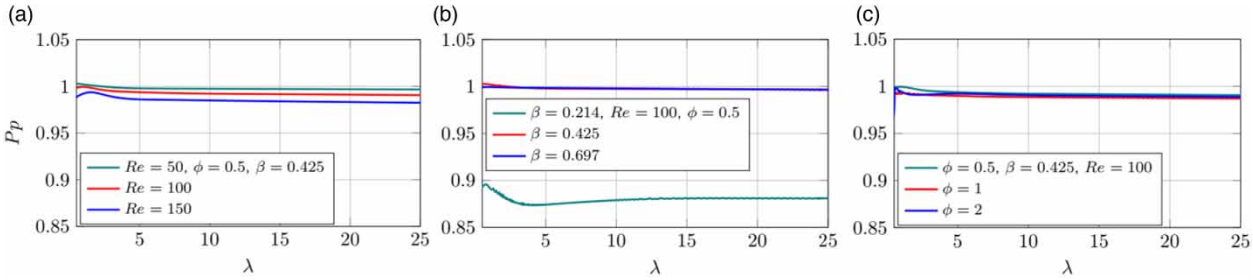

Figure 12 | Pressure power along the pipe axis for: (a) $Re = 50$, 100, and 150, with $\phi = 0.5$, and $\beta = 0.425$; (b) $\beta = 0.214$, 0.425, and 0.697, with $\phi = 0.5$ and $Re = 100$; and (c) $\phi = 0.5$, 1 and 2, $\beta = 0.425$, and $Re = 100$.

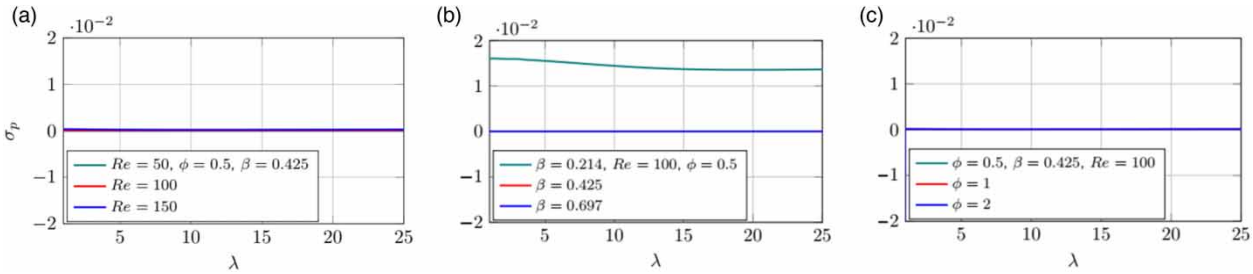

Figure 13 | Pressure distribution variance for: (a) $Re = 50$, 100, and 150, with $\phi = 0.5$, and $\beta = 0.425$; (b) $\beta = 0.214$, 0.425, and 0.697, with $\phi = 0.5$ and $Re = 100$; and (c) $\phi = 0.5$, 1 and 2, $\beta = 0.425$, and $Re = 100$.

the kinetic energy correction factor, as the velocity axial component, u, is predominant, with $\lambda (= x/D)$ being the dimensionless axial coordinate,

$$P_{\mathrm{P}} = \frac{\int_A pu \mathrm{d}A}{P_{\mathrm{up}} UA} \tag{14}$$

the power pressure, and the pressure distribution variance,

$$\sigma_{\mathrm{p}} = \frac{\int_A (p - P_{\mathrm{up}})^2 \mathrm{d}A}{P_{\mathrm{up}}^2 A} \tag{15}$$

where P_{up} is the mean pressure at the upstream section.

These plots confirm the above-mentioned results concerning the velocity and pressure distributions along the pipe axis. Precisely, in the considered cases, the behaviour of α, P_{p}, and σ does not depend on the values of the parameters characterising the extended PB.

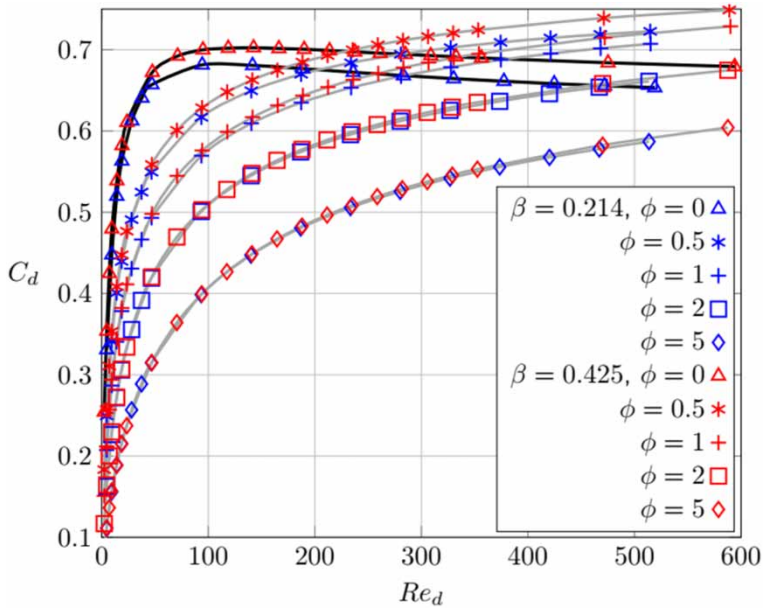

Figure 14 | Discharge coefficient, C_d, vs. orifice Reynolds number, Re_d, for different PB features.

A further quantity describing the global behaviour of the orifice, the discharge coefficient, C_d, given by Equation (6), has been evaluated. The curves reported in Figure 14 indicate the relevance of ϕ, β, and Re_d on C_d. Precisely, for a given Re_d, the smaller ϕ, the more relevant the role of β. For a given ϕ, the larger Re_d, the larger the influence of β.

Such a feature is the result of the mechanism of the vena contracta: the smaller ϕ, the more relevant the contraction. Moreover, according to Jankowski *et al.* (2008), the C_d behaviour vs. Re_d is different for sharp-edged orifices with respect to thick-walled ones and short tubes. Precisely, for a discrete PB, due to the effect of the vena contracta, C_d achieves a maximum value and then it slightly decreases. On the other hand, for an extended PB, C_d increases and then it reaches an asymptotic value. The maximum values of C_d vs. ϕ are reported in Figure 15.

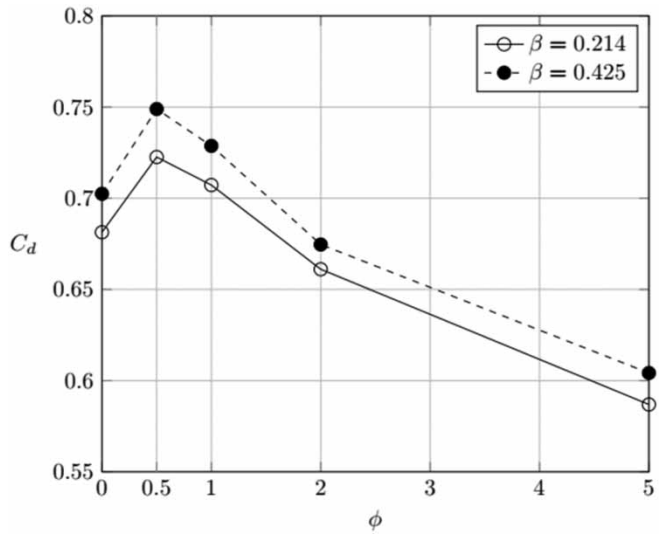

Figure 15 | Maximum values of C_d vs. ϕ for $\beta = 0.214$ and 0.425.

4. CONCLUSIONS

In this paper, the results of a three-dimensional (3D) CFD model describing the steady-state hydrodynamics of the laminar flow at an extended PB are presented.

As a necessary premise, in the first part of the paper, the results of the 3D CFD model are compared with the available experimental data. For all considered cases, there is a good fit between the numerical results and experimental data. Subsequently, the velocity and pressure distributions, provided by the 3D CFD model for a wide range of values of the Reynolds number, Re, length-to-diameter ratio, ϕ, and diameter ratio, β, are presented. Such results have been compared by considering both local and global parameters. In such a context, the different behaviour of sharp-edged orifices (discrete PBs) and thick-walled orifices and short tubes (extended PBs) is highlighted. The discharge coefficient, C_d, as an example, increases rapidly with Re_d for discrete PBs, whereas the maximum value is reached asymptotically for extended PBs. Such a behaviour has clear implications on the transient response of PBs and the related analysis performed within TTBTs.

ACKNOWLEDGEMENT

The authors are grateful for the support of Fundação para a Ciência e Tecnologia, research projects: Flow Dynamics in Storage Tanks (CPCA/A2/2568/2020) and IMiST – Improving Mixing in Storage Tanks for Safer Water Supply (PTDC/ECIEGC/32102/2017). The authors also acknowledge the support of the Università degli Studi di Perugia by the Fondo di Ricerca di Ateneo (Edizione 2021).

DATA AVAILABILITY STATEMENT

All relevant data are included in the paper or its Supplementary Information.

CONFLICT OF INTEREST

The authors declare there is no conflict.

REFERENCES

Alvi, S. H., Sridharan, K. & Lakshmana Rao, N. S. 1978 Loss characteristics of orifices and nozzles. *ASME Journal of Fluids Engineering* **100** (3), 299–307.

Brunone, B., Ferrante, M. & Meniconi, S. 2008 Discussion of 'Detection of partial blockage in single pipelines' by P. K. Mohapatra, M. H. Chaudhry. A. A. Kassem, and J. Moloo. *Journal of Hydraulic Engineering* **134** (6), 872–874.

Brunone, B., Capponi, C. & Meniconi, S. 2021 Design criteria and performance analysis of a smart portable device for leak detection in water transmission mains. *Measurement* **183**, 109844.

Denton, J. D. & Dawes, W. N. 1998 Computational fluid dynamics for turbomachinery design. *Proceedings of the Institution of Mechanical Engineers. Part C: Journal of Mechanical Engineering Science* **213** (2), 107–124.

Duan, H. F., Lee, P. J., Ghidaoui, M. S. & Tuck, J. 2014 Transient wave-blockage interaction and extended blockage detection in elastic water pipelines. *Journal of Fluids and Structures* **46**, 2–16.

Duan, W., Kirby, R., Prisutova, J. & Horoshenkov, K. V. 2015 On the use of power reflection ratio and phase change to determine the geometry of a blockage in a pipe. *Applied Acoustics* **87**, 190–197.

Fay, J. A. 1994 *Introduction to Fluid Mechanics*. MIT Press, London, UK.

Hasegawa, T., Suganuma, M. & Watanabe, H. 1997 Anomaly of excess pressure drops of the flow through very small orifices. *Physics of Fluids* **9** (1), 1–3.

Jankowski, T. A., Schmierer, E. N., Prenger, F. C. & Ashworth, S. P. 2008 A series pressure drop representation for flow through orifice tubes. *Journal of Fluids Engineering-T {ASME}* **130** (5), 1–7.

Johansen, F. C. 1997 Flow through pipe orifices at low Reynolds numbers. *Proceedings of the Royal Society of London. Series A* **126** (801), 231–245.

Keramat, A., Wang, X., Louati, M., Meniconi, S., Brunone, B. & Ghidaoui, M. S. 2019 Objective functions for transient-based pipeline leakage detection in a noisy environment: Least square and matched-filter. *Journal of Water Resources Planning and Management* **145** (10), 04019042.

Kiljanski, T. 1993 Discharge coefficient for free jets from orifices at low Reynolds number. *ASME Journal of Fluids Engineering* **115** (4), 778–781.

Lile, N. L. T., Jaafar, M. H. M., Roslan, M. R. & Azmi, M. S. M. 2012 Blockage detection in circular pipe using vibration analysis. *International Journal on Advanced Science, Engineering and Information Technology* **2** (3), 54–57.

Louati, M., Ghidaoui, M. S., Meniconi, S. & Brunone, B. 2018 Bragg-type resonance in blocked pipe system and its effect on the Eigen frequency shift. *Journal of Hydraulic Engineering* **144** (1), 04017056-04017051-04017011.

Martins, N. M. C., Carriço, N. J. G., Ramos, H. M. & Covas, D. I. C. 2014 Velocity-distribution in pressurized pipe flow using CFD: Accuracy and mesh analysis. *Computers & Fluids* **105**, 218–230.

Martins, N. M. C., Covas, D. I. C., Meniconi, S., Capponi, C. & Brunone, B. 2021 Characterisation of low-Reynolds number flow through an orifice: CFD results vs. laboratory data. *Journal of Hydroinformatics* **23** (4), 709–723.

Meniconi, S., Brunone, B. & Ferrante, M. 2011 In-line pipe device checking by short-period analysis of transient tests. *Journal of Hydraulic Engineering* **137** (7), 713–722.

Meniconi, S., Brunone, B. & Ferrante, M. 2012 Water-hammer pressure waves interaction at cross-section changes in series in viscoelastic pipes. *Journal of Fluids and Structures* **33**, 44–58.

Meniconi, S., Brunone, B., Ferrante, M. & Capponi, C. 2016 Mechanism of interaction of pressure waves at a discrete partial blockage. *Journal of Fluids and Structures* **62**, 33–45.

Meniconi, S., Brunone, B. & Frisinghelli, M. 2018 On the role of minor branches, energy dissipation, and small defects in the transient response of transmission mains. *Water-Sui* **10** (2), 187.

Papadopoulou, K. A., Shamout, M. N., Lennox, B., Mackay, D., Taylor, A. R., Turner, J. T. & Wang, X. 2008 An evaluation of acoustic reflectometry for leakage and blockage detection. *Proceedings of the Institution of Mechanical Engineers. Part C: Journal of Mechanical Engineering Science* **222** (6), 959–966.

Sahin, B. & Ceyhan, H. 1996 Numerical and experimental analysis of laminar flow through square-edged orifice with variable thickness. *Transactions of the Institute of Measurement and Control* **18** (4), 166–174.

Tu, X., Hrnjak, P. S. & Bullard, C. W. 2006 Refrigerant 134a liquid flow through micro-scale short tube orifices with/without phase change. *Experimental Thermal and Fluid Science* **30** (3), 253–262.

Yang, L., Fu, H., Liang, H., Wang, Y., Han, G. & Ling, K. 2019 Detection of pipeline blockage using lab experiment and computational fluid dynamic simulation. *Journal of Petroleum Science and Engineering* **183**, 106421–106410.

Zampaglione, D. 1969 Sul moto di una corrente laminare attraverso diaframmi (in Italian). *L'Energia Elettrica* **66**, 821–828.

First received 23 February 2023; accepted in revised form 21 October 2023. Available online 3 November 2023